NLR-TP-2002-461

Flow simulation using a boundary conforming discontinuous Galerkin finite element approach for the operational loads survey helicopter rotor in forward flight

O.J. Boelens, H. van der Ven, B. Oskam and A.A. Hassan

Nationaal Lucht- en Ruimtevaartlaboratorium

National Aerospace Laboratory NLR

NLR-TP-2002-461

Flow simulation using a boundary conforming discontinuous Galerkin finite element approach for the operational loads survey helicopter rotor in forward flight

O.J. Boelens, H. van der Ven, B. Oskam and A.A. Hassan*

* The Boeing Company (Mesa)

Customer:	National Aerospace Laboratory NLR
Working Plan number:	1.1.H.2h
Owner:	National Aerospace Laboratory NLR
Division:	Fluid Dynamics
Distribution:	Unlimited
Classification title:	Unclassified
	September 2002

Summary

The main issue explored in the present paper is the ability of the boundary conforming discontinuous Galerkin finite element approach to simulate the flow around a helicopter rotor in forward flight. A CFD flow solver based on this approach was developed by researchers from the National Aerospace Laboratory NLR and the Boeing Company. Comparison of the results of the simulation of an Operational Loads Survey helicopter rotor in forward flight using this DG algorithm with the results obtained using more conventional algorithms and wind tunnel measurements shows that the present DG approach yields the same or better agreement between CFD and experimental data. In the discussion of these results special attention will be given to the rotor trimming procedure developed by NLR and to the grid adaptation procedure.

Contents

(28 pages in total)

List of figures

List of tables

List of symbols

C_{Mx}	= moment around x-axis
C_{My}	= moment around y-axis
C_p	= surface pressure coefficient
C_T	= thrust coefficient
D	= rotor diameter
M	= local Mach number
M_{tip}	= tip Mach number
r	= radial distance along rotor blade
R	= rotor tip radius
x, y, z	= Cartesian coordinates
α_{TPP}	= tip-path plane angle
β_0	= collective flap angle
β_{1c}	= cosine-dependent flap angle
β_{1s}	= sine-dependent flap angle
$-\Delta C_p M^2$	= differential pressure
μ	= advance ratio
θ	= pitch angle
θ_0	= collective pitch angle
θ_{1c}	= cosine-dependent pitch angle
θ_{1s}	= sine-dependent pitch angle
ω	= vorticity
ψ	= azimuth angle
BVI	= blade-vortex interaction
DG	= discontinuous Galerkin
OLS	= Operational Loads Survey

This page is intentionally left blank.

1 Introduction

1.1 Blade vortex interaction background

The aerodynamics and acoustics of blade-vortex interaction (BVI) have been extensively studied in several large experimental programs, i.e., the OLS program (Refs. 8, 13 and 22), the AATMR program (Ref. 9), the HART program (Refs. 15 and 17) and the HELINOISE program (Ref. 14). These experimental programs, which were conducted in the German-Dutch Wind Tunnel (DNW), have provided a large set of aerodynamic and acoustic data, which has shed more light on a number of key parameters associated with complex blade-vortex interactions. It is nevertheless concluded from the HART program (Ref. 15) that more specific information, e.g., the vortex roll-up, the streamwise convection, the vortex ageing from the tip emission to blade encounter and eventually the vortex bursting, are required to completely understand the physics of blade-vortex interaction.

BVIs are caused by the close proximity between the rotor blades and the tip vortex wakes shed from the preceding blades or even the same blade. Strong interactions which result in large blade temporal pressure variations are caused by a tip vortex whose axis is parallel (or almost parallel) to the spanwise axis of the blade. BVIs predominantly occur in low-speed descent flight where the vortex wake remains near the rotor disk. However, BVI can also occur in forward flight for tandem rotor helicopters and during manoeuvres. Factors, that are known to impact the strength of BVI, are

(i)   The strength of the blade tip vortex,

(ii)   The average separation distance between the blade and the vortex wake, i.e., the miss distance, and

(iii)   The orientation of the vortex axis relative to the spanwise axis of the blade, i.e., parallel oblique or perpendicular.

BVI's take place on both the advancing and the retreating side of rotor disk. However, from an acoustics point of view the interactions on the advancing side are more dominant due to the locally higher Mach numbers. To accurately predict BVI noise, one must therefore accurately predict the location as well as the strength of the tip vortex wake since small changes in these parameters can result in significant differences in BVI noise levels.

1.2 State-of-the-art flow solver for helicopter rotors in forward flight

In Table 1 an overview is given of state-of-the-art Euler and Navier-Stokes flow solvers for the simulation of helicopter rotors in forward flight. The discontinuous Galerkin finite element flow solver discussed in this article is the only flow solver based on the boundary conforming ALE approach. The other codes apply the Chimera or overset approach, where sets of partially overlapping grids are used to cover the computational domain. At the grid overlaps flow interpolation is required, resulting not only in loss of the conservative property, but also

increasing the computational costs significantly. Loss of the conservative property is a major concern for the accuracy of the flow solver, and may result in dissipation of vorticity. Ochi (Ref. 10) and Pahlke (Ref. 12) report that on parallel vector machines 20% of the computing time is spent in the exchange of flow data between the different grids. Moreover, the use of overlapping grids involves a large amount of communication, which reduces the scalability of the Chimera or overset approach. Correlating the accuracy of the methods and the required flop count shows that the simulation of a rotor in forward flight is a petaflop problem for the algorithms on which these flow solvers are based. Hence, acceptable turn-around times can only be accomplished on massively parallel computers or by applying newly developed, more efficient algorithms (Ref. 21).

1.3   Outline of paper

In this paper the unique features and the accuracy of the discontinuous Galerkin finite element flow solver for capturing helicopter rotor wings are demonstrated.

First, the features of the discontinuous Galerkin (DG) finite element method are outlined. Next, the rotor trimming procedure for helicopters in forward flight as employed at NLR is presented. Also a section will be dedicated to the grid adaptation strategy used during the forward flight simulations. Following these discussions, the results of a simulation of the flow around the Operational Loads Survey helicopter rotor in forward flight are shown. These results are, where available, compared with experimental data. A summary and conclusions complete the report.

2   CFD algorithm

Based on the Euler equations, a unique predictive tool for rotorcraft flows has been developed by researchers from the National Research Laboratory, NLR, in the Netherlands and the Boeing Company. This CFD flow solver is based on a discontinuous Galerkin (DG) finite element discretization of the unsteady compressible Euler equations (Refs. 4, 5, 18 and 19).

Discontinuous Galerkin finite element methods use a discontinuous function space to approximate the exact solution of the Euler equations. The discontinuous Galerkin finite element method is a mixture of a finite element and an upwind finite volume method. The flow domain is discretized into a large number of hexahedral elements. The polynomial expansions of the flow field variables are purely element-based and there will be, in general, a discontinuity in the flow field variables across element faces, with as magnitude the truncation error in the polynomial representation. This discontinuity at element faces is interpreted as a one-dimensional Riemann problem, which is used to obtain a unique definition of element face fluxes. The use of a Riemann problem in the flux calculation introduces upwinding into the

finite element discretization. An introduction to these DG methods is provided in the lecture notes of a NATO special course on *Higher Order Discretization Methods in CFD* (Ref. 4).

A unique feature of the DG finite element method is that equations are solved not only for the mean flow field, but also for the flow field gradients. This results in a very compact scheme, because it is not necessary to reconstruct the flow field gradients, necessary to achieve second-order accuracy, using data in neighboring elements. The present finite element method has excellent shock capturing capabilities and is easy to parallelize since there is only limited communication between neighboring elements.

The DG finite element method has an inherent ability to handle adaptivity strategies since the refining and de-refining of the grid is done without taking into account the continuity restrictions of conventional CFD methods (Refs. 6, 18, 19 and 20). At this point it should be remarked that in the present research h-refinement is utilized to construct a locally isotropic grid from an anisotropic, initial grid. The anisotropy (elements having large aspect ratios) of the initial grid is often a concomitant feature of efficient, boundary conforming structured grids.

Dynamic motions of multiply bodies are simulated using a single, deforming, boundary conforming mesh. The Euler equations on such a mesh are discretized simultaneously in space and time, leading to an Arbitrary Lagrangian Eulerian (ALE) formulation, which incorporates the grid velocities in the flow formulation. Consequently, a conservative scheme that has the same accuracy as the standard DG method for a rigid mesh is obtained. In addition to the governing equations used to evaluate the flow field gradients in space, equations are also solved for the flow field temporal gradients. A clear advantage of this solution method is manifest in its ability to use non-uniform time steps without sacrificing temporal accuracy. For unsteady rotor computations (e.g., for a rotor in forward flight), this feature can be used to reduce the overall required CPU time (number of azimuthal steps) for the computation of one rotor revolution. This efficiency, of course, is achieved at the expense of increased memory requirements due to the additional equations being solved for the temporal derivatives of the flow field variables. The equations are solved implicitly by introducing a pseudo-time and marching the solution to a steady state using a standard FAS multigrid algorithm. In this way, the ALE method using a single deforming mesh retains the excellent parallelizability properties of the explicit DG method on rigid meshes.

It should be noted that an extension of the DG algorithm from the Euler equations to the Navier-Stokes equations is feasible while retaining the excellent adaptivity and parallelizability properties of the method (Ref. 1).

3 Rotor trimming

A fair comparison between experimental data and numerical simulations can only be obtained if for both cases the helicopter rotor is operating at the same thrust coefficient. Since the experimental thrust coefficient is fixed, the thrust coefficient obtained during the simulations has to be adjusted in such a way that it matches the experimental one. This adjustment or trimming procedure means that the pitch, flap and lead-lag schedule are modified in such a way that the thrust coefficient equals the desired value and the rotor plane moment coefficients around the x-axis and the y-axis are zero.

For a helicopter rotor the pitch schedule is given by

$$\theta = \theta_0 + \theta_{1c} \cos \psi + \theta_{1s} \sin \psi$$

where ψ is the azimuth angle. Note that in the current simulation of the Operational Loads Survey helicopter rotor in forward flight the flap schedule has not been modified and no lead-lag schedule has been used. In that case the revolution-averaged thrust coefficient C_T and the rotor plane moment coefficients C_{Mx} and C_{My} depend on the collective pitch angle θ_0, the cosine-dependent pitch angle θ_{1c} and the sine-dependent pitch angle θ_{1s}. The revolution-averaged thrust coefficient C_T mainly depends on the collective pitch angle θ_0, the revolution-averaged moment coefficient around the y-axis C_{My} mainly depends on the cosine-dependent pitch angle θ_{1c} and the revolution-averaged moment around the x-axis C_{Mx} mainly depends on sine-dependent pitch angle θ_{1s}. Note that the x-axis points from the rotor to the tail-rotor, and that the y-axis points right looking from the tail-rotor to the rotor (pilot's view). The effect of adjusting the rotor collective and cyclic pitch on the thrust coefficient and rotor plane moment coefficients follows from taking the linear term of the Taylor-expansion of these coefficients, i.e.,

$$\begin{pmatrix} C_T \\ C_{My} \\ C_{Mx} \end{pmatrix} (\theta_0 + \Delta\theta_0, \theta_{1c} + \Delta\theta_{1c}, \theta_{1s} + \Delta\theta_{1s}) \approx$$

$$\begin{pmatrix} C_T \\ C_{My} \\ C_{Mx} \end{pmatrix} (\theta_0, \theta_{1c}, \theta_{1s})$$

$$+ \begin{bmatrix} \dfrac{\partial C_T}{\partial \theta_0} & \dfrac{\partial C_T}{\partial \theta_{1c}} & \dfrac{\partial C_T}{\partial \theta_{1s}} \\ \dfrac{\partial C_{My}}{\partial \theta_0} & \dfrac{\partial C_{My}}{\partial \theta_{1c}} & \dfrac{\partial C_{My}}{\partial \theta_{1s}} \\ \dfrac{\partial C_{Mx}}{\partial \theta_0} & \dfrac{\partial C_{Mx}}{\partial \theta_{1c}} & \dfrac{\partial C_{Mx}}{\partial \theta_{1s}} \end{bmatrix} (\theta_0, \theta_{1c}, \theta_{1s}) \begin{pmatrix} \Delta\theta_0 \\ \Delta\theta_{1c} \\ \Delta\theta_0 \end{pmatrix}$$

Here $\Delta\theta_0$, $\Delta\theta_{1c}$ and $\Delta\theta_{1s}$ indicate the small changes in the collective, cosine-dependent and sine-dependent cyclic pitch, respectively. The coefficients in the matrix are the sensitivities of the thrust coefficient and rotor plane moment coefficients to changes in the collective and cyclic

pitch, with the diagonal terms being the dominant ones. These coefficients can be obtained by performing three additional simulations with small variations of the collective pitch, the cosine-dependent cyclic pitch and the sine-dependent cyclic pitch.

4 Grid adaptation

The general idea behind grid adaptation for helicopter rotor flows is that in order to minimise the numerical diffusion of the vorticity and the numerical dissipation in a vortex, the grid within the vortex should be as isotropic, as uniform and as refined as possible.

The grid adaptation algorithm consists of the following parts:

(i)   The grid adaptation sensor. Basically, two types of sensors are available: (1) sensors that measure differences of flow quantities across element faces, and (2) sensors that measure the magnitude of a flow variable in an element. An example of the first sensor type is the standard shock sensor, which measures flow 'gradients' (actually differences) of the five conserved variables and the total pressure loss across element faces. An example of the second sensor type is the vortex sensor based on, for example, the vorticity magnitude. In addition to these sensors one can also use a grid quality sensor, i.e., a sensor that measures the jump in the mesh width in the direction normal to the element face, an anisotropy sensor, i.e., a sensor that measures the anisotropy (aspect ratios) of an element, and, a uniformity sensor, i.e., a sensor that measures the mesh width in each co-ordinate direction.

(ii)   The grid adaptation type. The two basic types of grid adaptation are isotropic and anisotropic grid adaptation. If a sensor contains directional information (such as the shock sensor), anisotropic grid adaptation is used. The element is adapted in the direction associated with the gradient. If a sensor contains no directional information, isotropic adaptation is used.

(iii)   The grid adaptation control. The adaptation control determines for example the adaptation frequency and the percentage of elements that will be refined or de-refined.

During the forward flight simulation the grid adaptation sensor used was a combination of the vortex sensor based on the vorticity magnitude with the anisotropy sensor or the uniformity sensor, resulting in uniform meshes of specified width (typically 0.005 rotor diameters, i.e., 2.5 times the required width reported by Caradonna (Ref. 3)) in the vortex.

With respect to the adaptation frequency for time-accurate, time-periodic simulations, such as the simulation of a helicopter rotor in forward flight, two options exist: (i) simply adapt the grid at each implicit time step or, (ii) integrate the grid adaptation sensor over a complete period (e.g., corresponding to a user-specified azimuthal travel) and adapt the mesh based on this integrated sensor after the completion of the period. Both strategies have advantages and

disadvantages. The first strategy is more efficient in terms of number of elements, since elements are both created and removed at each implicit time step. Moreover, with the grid being adapted during the period, faster convergence to a periodic flow solution is achieved. However, since grid adaptation results in a dynamic load-balancing problem, for which currently no scalable algorithms are known, the parallel efficiency of the flow solver will deteriorate. The second resembles the classical adaptation strategy used in steady state problems. This method retains the parallel efficiency of the flow solver, but since the same adapted grid is used for all time steps the number of elements is larger than in the first strategy. A compromise between the two grid adaptation strategies is the following. At each implicit, time step the mesh is only 'refined' based on the instantaneous grid adaptation sensor and adaptation type. However, no elements are removed as is done in the first strategy. This effectively integrates the sensor in time, and allows for faster convergence to the periodic flow solution. For the simulation of the helicopter rotor in forward flight this compromise has been used.

5 Operational Loads Survey helicopter rotor simulations

5.1 General description

The Operational Loads Survey (OLS) helicopter rotor is a 1/7-scale model of the two-bladed AH-1 helicopter rotor, see Ref. 2. The planform of the AH-1G/OLS rotor is rectangular and the blade is a modified BHT-540 section. The airfoil has been modified in order to accommodate full-scale pressure instrumentation during the experiment. The resulting thickness is 9.71%. The diameter of the rotor is 1.916m and the chord length is 0.1039m. The blades have a blade root cut-out at 18.2% of the rotor radius. The rotor blades are twisted 10 degrees from the blade root to the blade tip. In rest the blade pitch angle at the 75% radial station is zero. All blade angles are specified with respect to this station. The Operational Loads Survey helicopter rotor blades pitch about quarter-chord.

The flow around the Operational Loads Survey helicopter rotor in forward flight reported in this publication has been simulated for the flow conditions of RUN 3020 (Ref. 2), i.e. a tip Mach number of 0.664, an advance ratio of 0.164, a thrust coefficient of 0.0054 and a tip-path plane angle of 2 degrees. This case corresponds to the following flight conditions:

(i)   A forward velocity of the rotor of 72 knots, i.e. 37 m/s, and

(ii)   A rate of descent of approximately 400 ft/min, i.e. 2 m/s.

5.2 Computational grid

For the above described OLS helicopter rotor a multi-block structured grid has been generated. To enable the generation of a high quality grid near the blade tips the blade geometry has been

complemented with a cap (by revolving the modified BHT-540 tip profile around its axis). The requirements for the grid generation are:

(i)   To minimise radiation of the grid resolution near the blades to the far field as much as possible, and

(ii)   To create a grid as uniform as possible.

The resulting multi-block topology satisfying both requirements is illustrated in Fig. 1. In order to minimise radiation of the blade to the far field, (i) an O-type block structure around the blade in the chordwise direction has been used, see Fig. 1(d), and (ii) the grid lines have been folded around both tip and root caps in the spanwise direction, i.e. the grid lines first are parallel to the blade leading edge, then parallel to the blade tip, parallel to the blade trailing edge and finally parallel to the blade root, see Figs. 1(a) and (b). The region between the blades (i.e., the hub region) has been filled by two blocks, see Fig. 1(a). Since for a helicopter rotor in forward flight the position of the vortex a priori is not known the grid both above and below the rotor has been made as uniform as possible, see Fig. 1(c). It should be noted that a collective pitch angle θ_0 of 6.14 degrees (see Table 2: Strawn[15]) has been included in the initial grid, i.e., the blade pitch angle at the 75% radial station equals θ_0. Therefore the grid is as optimal as possible for the blades at rest.

The resulting initial multi-block grid consists of 72 blocks, with a total of 244,224 elements.

5.3   Rotor trimming

Since trim simulations are computationally intensive for Euler/Navier-Stokes-based methods, a lifting line vortex method (CAMRAD/JA, Ref. 7) has been used as a first estimate to calculate the sensitivities of the thrust coefficient.

To obtain the complete sensitivity matrix enabling the proper trimming of the helicopter rotor, the above described method developed at NLR has been used. Three additional simulations, where either the collective pitch angle, the cosine-dependent cyclic pitch angle or the sine-dependent cyclic pitch angle were increased by one degree, have been performed with the present Euler-based DG method (see Table 2: Schedules 2[a], 2[b], 2[c]). These simulations, using an azimuthal step of 10 degrees, start from a periodic solution (obtained by Schedule 2) and are continued until the new solution also is periodic. For the present simulation, these simulations only consisted of one full revolution due to the small transient (only a quarter of a revolution). The second half of this revolution has been used to obtain the force and moments needed for the sensitivity calculations (see Table 3).

5.4   Results

The complete simulation consisted of several revolutions (see Tabel 2). Note that different azimuthal increments have been used during the simulation. The large amount of revolutions used during the simulation is caused by the fact that

(i)   The flow solver was under constant development during the first phase of the research (Schedule 1), and

(ii)   Accurate rotor trimming data has been unavailable.

Under normal, non-development conditions three revolutions would suffice to perform a simulation of the flow around the OLS helicopter rotor in forward flight including grid adaptation.

During the simulation the grid has been adapted twice, i.e., the first time during the second half of the third revolution using Schedule 1, and the second time during the second full revolution using Schedule 3. During the first adaptation (lasting only half of a revolution) the vortex sensor based on the vorticity magnitude has been used in combination with the anisotropy sensor, resulting in a grid of 488,026 elements (see Fig. 2). During the second adaptation the vortex sensor based on the vorticity magnitude has been used in combination with the uniformity sensor. The grid in the vortex was adapted to a uniform mesh width equal to 0.005D. At each implicit time step the mesh has only been refined. Since no elements were removed, in this manner the vortex sensor was effectively integrated in time. After adaptation the grid contains 1,297,729 elements (see Fig. 2).

Fig. 3 shows the differential pressure $-\Delta C_p M^2$ at the three percent chordwise station at r/R=0.750, 0.80, 0.85, 0.91 and 0.975 for the experiment and the three schedules used. Here C_p is the surface pressure coefficient and M is the local Mach number. The delta-symbol indicates that the difference between the surface pressure coefficient on the upper and lower surface of the rotor blade is taken. Note that the presented data was obtained during the last full revolution using the respective schedules. In Fig. 3(e) also the results of Ref. 16 are shown. Strawn's results are obtained on a grid consisting of 1.8 million grid points using a constant increment of the azimuth angle of 0.25 degrees. It can be seen that going from Schedule 1 to Schedule 3 the results get significantly closer to the experiment. The agreement between the differential pressures obtained using Schedule 3 and the experiment is generally good. The overall agreement improves with increasing radial position r/R. Several blade-vortex interaction events can be observed. Comparing this figure with previously reported Euler and Navier-Stokes simulations for the Operational Loads Survey helicopter rotor in forward flight (Refs. 11 and 16), one can see that with the present method a considerable improvement has been obtained. Although the effects of trimming and grid adaptation intertwine during these simulations, the global improvement in the differential pressure distributions can be attributed to the trimming and the local improvement, i.e., the additional BVI events, to the grid adaptation.

The obtained revolution-averaged thrust coefficient and rotor plane moment coefficients are shown in Tab. 3. The revolution-averaged thrust coefficient for Schedule 3 is slightly higher than the experimental value of 0.0054, whereas the revolution-averaged rotor plane moment coefficients are small (compare with Ref. 16).

In Fig. 4, the sectional lift, the differential pressure at the three percent chordwise station and the derivatives of the sectional lift and the differential pressure at the three percent chordwise station with respect to the azimuth angle are shown for Schedule 3. On both the advancing side and the retreating side the present simulation finds two interactions. Starting form $\psi=0°$ and looking in counter clockwise direction, the rotor blade first interacts parallel (PI) with a vortex originating from the blade itself, next it interacts perpendicular (PPI) with the vortex originating from the other blade, then there is once more an interaction with the vortex originating from the other blade which initially is perpendicular but develops into an oblique interaction (OI), and finally the blade interacts with a vortex originating from itself. This final interaction starts as a parallel interaction (PI) but develops into an oblique interaction (OI).

On the advancing side the angular position of the interactions is slightly mispredicted (see also Fig. 3). The slope of the differential pressure is, however, predicted correctly (except for the radial station closest to the tip cap). On the retreating side, both the slope and azimuthal position of the oblique interaction is predicted correctly. For the parallel interaction on the retreating side both the differential pressure level and slope is mispredicted.

In this figure the effect of the root vortices can be clearly seen by the interactions around the zero azimuth angle. It is obvious that the presence of these vortices, which are not present in the experiment due to a different geometry in the hub region, influences the solution.

Fig. 5 shows vorticity magnitude contours for the Operational Loads Survey on cross-sectional planes seen from above the rotor at azimuthal steps of 15 degrees. The airflow is from left to right. Six cross-sectional planes located at z/R=-0.15, -0.10, -0.05, 0.0, 0.05 and 0.1 have been used to create these figures. Here z denotes the direction normal to the rotor plane. The transparency of the cross-sectional planes increases with increasing z-co-ordinate. These figures visualise the time-dependent flow pattern around the Operational Loads Survey helicopter rotor in forward flight. After the vortices are created at the blade tips, they are convected downstream. During this downstream convection the blade vortex interactions occur. It can be seen that as soon as the tip vortices leave the disk-shaped adapted grid region having elements widths of 0.005D, the vortices disappear. This disappearing can be attributed to

(i)   The higher physical CFL number in this region which results in diffusion of vorticity, and

(ii)   The increased element widths which results in dissipation of vorticity.

The presence of the root vortices can also be clearly seen in these figures.

6   Summary

The discontinuous Galerkin finite element algorithm based on a boundary conforming ALE formulation in conjunction with unstructured grid refinement of hexahedral grids has been used for the simulation of the unsteady flow field around the two-bladed Operational Loads Survey (OLS) helicopter rotor in forward flight for a BVI condition.

The grid on which this simulation has been performed has been especially designed to minimise the radiation for the blades to the far field. This has been achieved by folding the grid lines around the blades. The helicopter rotor has been trimmed using the rotor trimming procedure developed by the National Aerospace Laboratory NLR to obtain a fair comparison with the experiment. Furthermore, the grid has been adapted to a width of 0.005 in all three co-ordinate directions in the vortex. Since the DG method also solves for the variation within the elements, this width corresponds to 2.5 times the required width reported on in Ref. 3.

The differential pressure at the three percent chordwise station obtained during the simulation has been compared with the experimental one. The agreement is generally good. Moreover, a considerable improvement has been obtained compared to previously reported Euler and Navier-Stokes simulations (Refs. 11 and 16). On the advancing side two BVI events have been observed, i.e., one parallel interaction and one perpendicular interaction. Although the angular position of the interactions is slightly mispredicted, the slope of the differential pressure, which is a measure of the radiated noise, is predicted correctly (except for the outermost radial station that is close to the tip cap). On the retreating side, two interactions may be observed, i.e., one oblique interaction and one parallel interaction. The azimuthal position and the slope of the oblique interaction are predicted correctly. For the parallel interaction the differential pressure levels and slopes are, however, mispredicted. Note also that strong vortices coming from the root tips have been observed. The presence of these vortices may jeopardise the solution.

7   Conclusions

The main issue explored in the present paper is the ability of the boundary conforming discontinuous Galerkin finite element approach to simulate the flow around a helicopter rotor in forward flight. Comparison of the results of the simulation of an Operational Loads Survey helicopter rotor in forward flight using this DG algorithm with the results obtained using more conventional algorithms (Refs. 11 and 16) shows that the present DG approach yields the same or better agreement between CFD and experimental data.

For accurate prediction of the flow around a rotor in forward flight, it was concluded that trimming of the rotor is of utmost importance. The trimming procedure developed at NLR resulted in substantially improved differential pressure distributions when compared with those presented in the literature (Refs. 11, 12 and 16). Pahlke (Ref. 12) stresses the importance of proper trimming by the following observation: 'It was shown that the viscous effects are important for the prediction of the global forces but the effect of trim is even more important'.

In the introduction it was remarked that the accurate simulation of a helicopter rotor in forward flight is a petaflop problem for the algorithms on which the state-of-the-art flow solvers are based. In Ref. 21 a new algorithm is introduced that significantly reduces the computing time required to reach a time-periodic solution. The application of this algorithm will lead to time-efficient simulations for a helicopter rotor in forward flight. A comparison between this algorithm and the algorithms used in the state-of-the-art flow solvers shows that an order of magnitude reduction in turnaround time can be achieved at the expense of an order of magnitude increase in memory use.

Acknowledgements

References

[1] Atkins, H.L., and C.W. Shu, "Analysis of the Discontinuous Galerkin Method to the Diffusion Operator," AIAA Paper 1999-3306, 1999.

[2] Boxwell, D.A., Schmitz, F.H., Splettstoesser, W.R. and Schultz, K.J., "Helicopter Model Rotor-Blade Vortex Interaction Impulsive Noise: Scalability and Parametric Variations," Journal of American Helicopter Society, 32, 1987, 3-12.

[3] Caradonna, F.X., "Development and Challenges in Rotorcraft Aerodynamics," AIAA Paper 2000-0109, 2000.

[4] Cockburn, B., "Discontinuous Galerkin Methods for Convection-Dominated Problems," High-order methods for computational physics, edited by T. Barth and H. Deconinck, Lecture Notes in Computational Science and Engineering, 9, Springer Verlag, 1999.

[5] Cockburn, B., Karniadakis, G. and Shu, C.-W., "An Overview of the Development of Discontinuous Galerkin Methods," Lecture Notes in Computational Science and Engineering, Vol. 11, Springer Verlag, 1999.

[6] Devine, K.D. and Flaherty, J.E., "Parallel adaptive hp-refinement techniques for conservation laws," Applied Numerical Mathematics: Transactions of IMACS, 20, 4, 1996, 367-386

[7] Hassan, A.A., Charles, B.D, Tadghighi, H. and Burley, C., "A Consistent Approach for Modeling the Aerodynamics of Self-Generated Rotor Blade-Vortex Interactions," Journal of the American Helicopter Society, April 1996, 74-84.

[8] Kondo, N., Ochi, A., Nakamura, H., Aoyama, T., Saito, S. and Yamakawa, E., "Validation of Rotor Aerodynamic and Acoustic Prediction Methods using ATIC 2nd Model Rotor," Paper presented at 26th European Rotorcraft Forum, The Hague, The Netherlands, 2000.

[9] Lorber, P.F., "Aerodynamic results of a pressure-instrumented model rotor test at DNW," Journal of the American Helicopter Society, 1991, 66-76.

[10] Ochi, A., Aoyama, T., Saito, S., Shima, E. and Yamkawa, E., "BVI noise Predictions by Moving Overlapped Grid Method," Paper presented at 55th American Helicopter Society Annual Forum, Montreal, Canada, 1999.

[11] Pahlke, K., "Berechnung von Strömungsfeldern um Hubschrauberrotoren im Vorwärtsflug durch die Lösung der Euler-Gleichungen," Forschungsbericht 1999-22, Deutsches Zentrum für Luft- und Raumfahrt e. V., 1999.

[12] Pahlke, K. and Chelli, E., "Calculation of Multiblade Rotors in Forward Flight Using a 3D Navier-Stokes Method," Paper presented at 26th European Rotorcraft Forum, The Hague, The Netherlands, 2000.

[13] Shockey, G.A., Williamson, J.W. and C.R. Cox, "Helicopter aerodynamics and structural loads survey," Paper presented at 32nd American Helicopter Society Annual Forum, Washington, DC, USA, 1976.

[14] Splettstoeser, W.R., Niesl, G., Cenedese, F., Nitti, F. and D.G. Papnikas, "Experimental results of the European HELINOISE aeroacoustic rotor test," Journal of the American Helicopter Society, 1995, 3-14.

[15] Splettstoeser, W.R., Kube, R., Wagner, W., Seelhorst, U., Boutier, A., Micheli, F., Mercker, E. and K. Pengel, "Key results from a higher harmonic control aeroacoustic rotor test (HART)," Journal of the American Helicopter Society, 1997, 58-78.

[16] Strawn, R.C., Ahmad, J. and Duque, E.P.N., "Rotorcraft Aeroacoustics Computations with Overset-Grid CFD Methods," Paper presented at the 54th American Helicopter Society Annual Forum, Washington, DC, USA, 1998.

[17] Tung, C., Gallman, J.M., Kube, R., Wagner, W., van der Wall, B., Brooks, T.F., Burley, C.L., Boyd Jr., D.D., Rahier, G. and P. Beaumier, "Prediction and measurement of blade-vortex interaction loading," Proceedings CEAS/AIAA, 95-051, 1995, 365-375.

[18] van der Vegt, J.J.W. and van der Ven, H., "Discontinuous Galerkin Finite Element Method with Anisotropic Local Grid Refinement for Inviscid Compressible Flow," J. Comput. Phys., 140, 1998, 1-32.

[19] van der Vegt, J.J.W., and van der Ven, H., "Space-Time Discontinuous Galerkin Finite Element Method With Dynamic Grid Motion For Inviscid Compressible Flow. Part I. General Formulation," to appear in J. Comput. Phys., 2002.

[20] van der Ven, H. and van der Vegt, J.J.W., "Accuracy, Resolution, and Computational Complexity of a Discontinuous Galerkin Finite Element Method," Lecture Notes in Computational Science and Engineering, Vol. 11, Springer Verlag, 1999.

[21] van der Ven, H., Boelens, O.J. and Oskam, B., "Multitime multigrid convergence acceleration for periodic problems with future applications to rotor simulations," International Parallel CFD 2001 Conference, Eds. P. Wilders et al., North-Holland Elsevier, 2002.

[22] Yu, Y.H., Tung, C., Gallman, J., Schultz, K.J., van der Wall, B., Spiegel, P. and B. Michea, "Aerodynamics and acoustics or rotor blade-vortex interactions," Journal of Aircraft, 32, 1995, 970-977.

Code name	Main technique	Flow conservation	Adaptivity	Scalability	Accuracy
ASTRA-OG[8,10]	Chimera/Overset	○	-	-	+
FLOWER[11]	Chimera/Overset	○	-	-	○
FLOWER[12]	Chimera/Overset	○	-	-	○
OVERFLOW[16]	Chimera/Overset	○	○	-	○
DG flow solver	Boundary conforming	+	+	○	+

Code name	Rotor type	Number of blades	Number of grid points ($\times 10^6$)	Computing time for one revolution	Flop count ($\times 10^{12}$)
ASTRA-OG	ATIC AT2	5	17.0	20 hours on NWT/30	1100
FLOWER	OLS	2	1.4	107 hours on Cray J916/1	58
FLOWER	ONERA 7AD	4	2.0	23.5 hours on NEC SX-5/1	135
OVERFLOW	OLS	2	1.8	15 hours on Cray C-90/1	16
DG flow solver	OLS	2	1.2	20 hours on NEC SX-5/8	1150

Table 1: Qualitative comparison and computing times of existing Euler and Navier-Stokes helicopter rotor codes for forward flight simulations. NWT: Numerical Wind Tunnel (parallel vector machine with 1.7 Gflop/s peak per processor), Cray J916: parallel vector machine with 0.5 Gflop/s peak per processor, Cray C-90 parallel vector machine with 1 Gflop/s peak per processor, NEC SX-5 parallel vector machine with 8 Gflop/s peak per processor. The flop counts are estimated from the computing times and an assumed sustained performance of 30 % on vector processors.(- = unsatisfactory, ○ = fair, + = good). Data is taken from Kondo (Ref. 8), Ochi (Ref. 10), Pahlke (Refs. 11 and 12) and Strawn (Ref. 16).

	$\theta_0[°]$	$\theta_{1c}[°]$	$\theta_{1s}[°]$	$\beta_0[°]$	$\beta_{1c}[°]$	$\beta_{1s}[°]$	No. of revolutions	$\Delta\psi[°]$
Schedule 1	6.53	0.90	-1.39	2.40	-1.00	0.00	4	0.25-5.00
Schedule 2	6.98	1.95	-3.20	2.40	-1.00	0.00	1	5.00
Schedule 2[a]	7.98	1.95	-3.20	2.40	-1.00	0.00	1	10.00
Schedule 2[b]	6.98	2.95	-3.20	2.40	-1.00	0.00	1	10.00
Schedule 2[c]	6.98	1.95	-4.20	2.40	-1.00	0.00	1	10.00
Schedule 3	6.62	2.81	-2.19	2.40	-1.00	0.00	3.5	1.25
Strawn[15]	6.14	0.90	-1.39	0.50	-1.00	0.00	-	0.25

Table 2: Pitch and flap angles and simulation data used in the simulation of the Operational Loads Survey helicopter rotor in forward flight.

	C_T ($\times 10^3$)	C_{Mx} ($\times 10^3$)	C_{My} ($\times 10^3$)
Experiment	5.40	0.00	0.00
Schedule 1	5.440	0.161	0.519
Schedule 2	5.444	-0.218	0.222
Schedule 2[a]	6.282	-0.071	0.236
Schedule 2[b]	5.557	-0.196	-0.104
Schedule 2[c]	5.288	-0.468	0.159
Schedule 3	5.553	0.037	-0.112
Strawn[16]	5.43	0.11	0.41

Table 3: Force and moment data from the simulation of the Operational Loads Survey helicopter rotor in forward flight. Experimental data is taken from Strawn (Ref. 16).
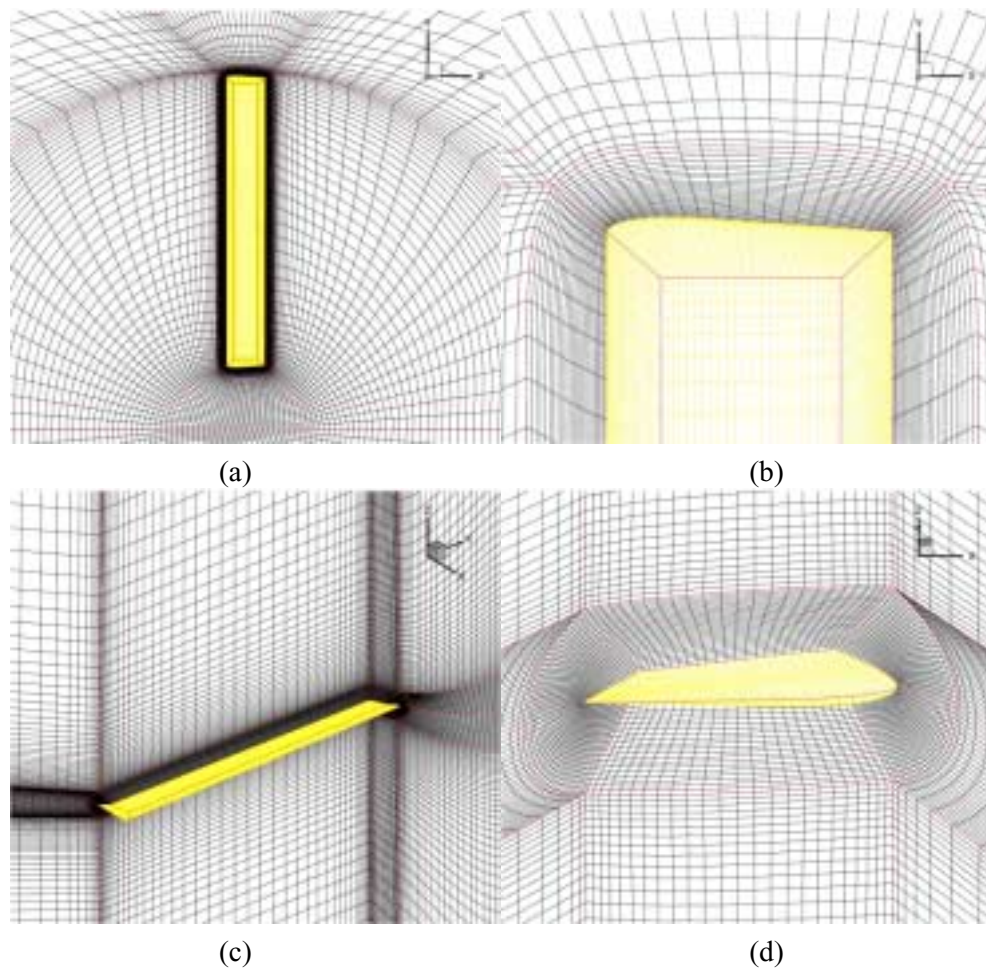
(a)

(b)

(c)

(d)

Figure 1: The initial OLS helicopter grid: top view of the grid surrounding the rotor blade (a), detail of the grid near the blade tip (b), front view of the grid surrounding the rotor blade (c) and side view of the grid near the blade tip (d). The rotor is coloured yellow. The block boundaries are coloured red.
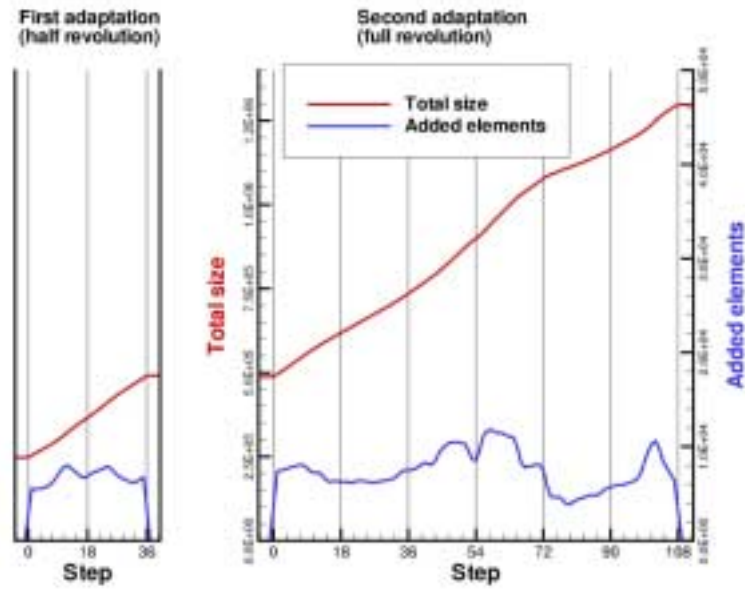
Figure 2: Total grid size and number of added elements for the first adaptation (lasting a half revolution) using the anisotropy sensor and the second adaptation (lasting a full revolution) using the uniformity sensor.
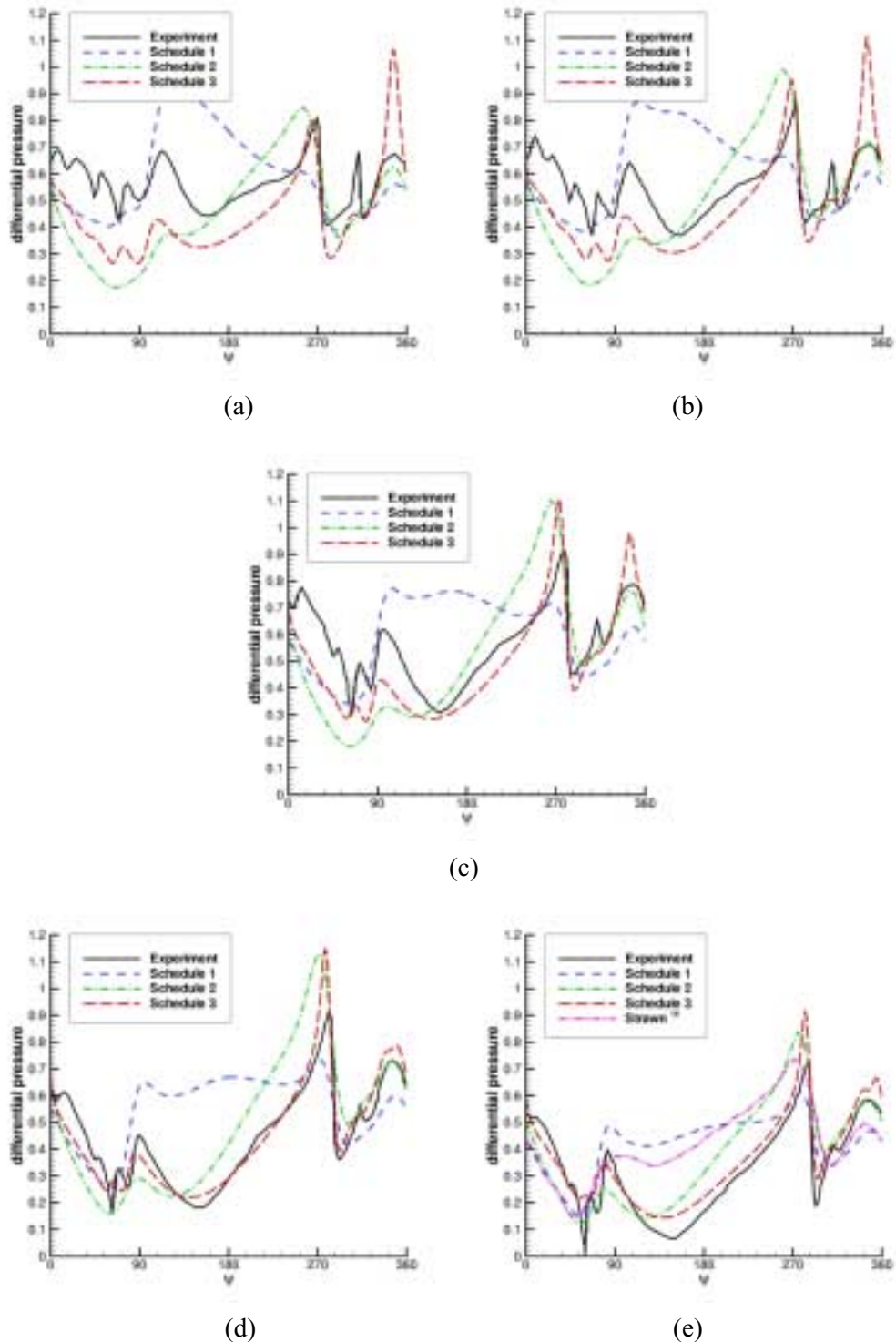
(a)

(b)

(c)

(d)

(e)

Figure 3: Differential pressure $-\Delta C_p M^2$ at the three percent chordwise station at the radial stations r/R=0.75 (a), 0.80 (b), 0.85 (c), 0.91 (d) and 0.975 (e) for the Operational Loads Survey helicopter rotor in forward flight.
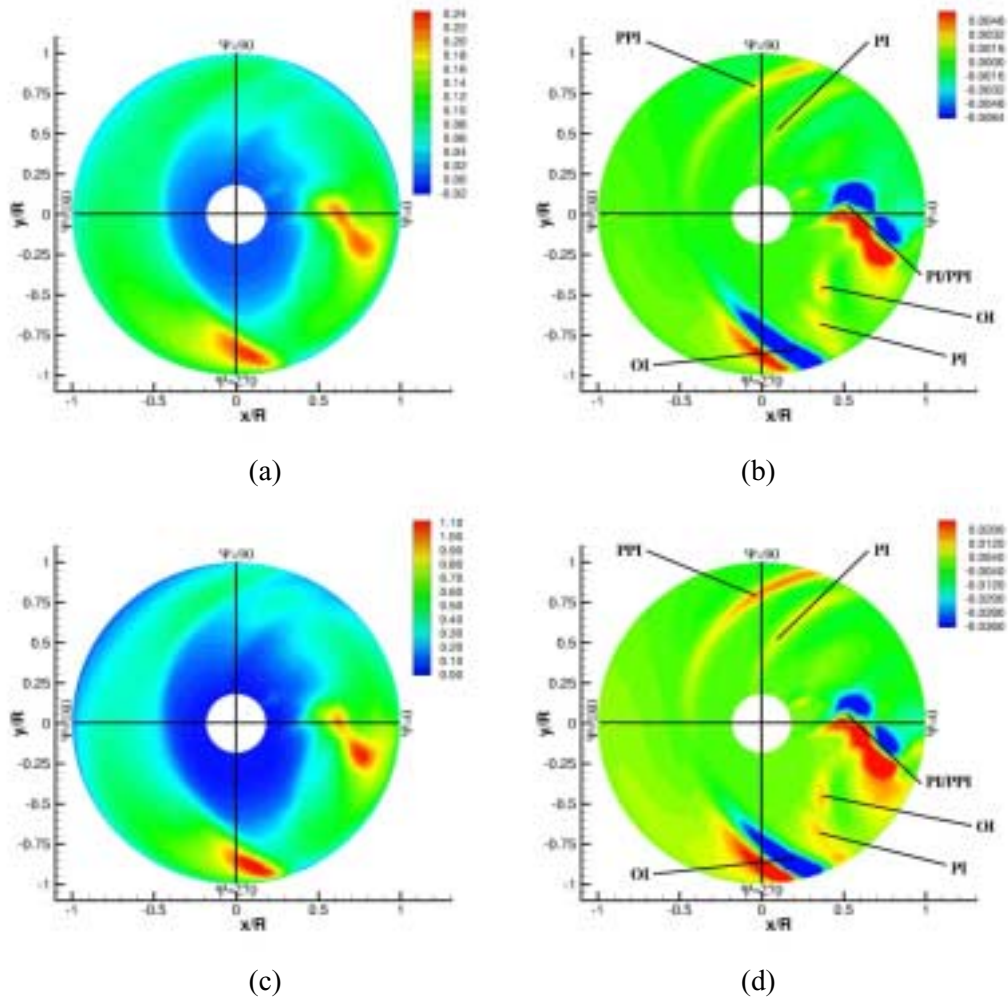
(a)

(b)

(c)

(d)

Figure 4: The sectional lift (a), the derivative of the sectional lift with respect to the azimuth angle ψ (b), the differential pressure $-\Delta C_p M^2$ at the three percent chordwise station (c) and the derivative of the differential pressure $-\Delta C_p M^2$ at the three percent chordwise station with respect to the azimuth angle ψ (d) for Schedule 3; PI: parallel interaction, PPI: perpendicular interaction, OI: oblique interaction.
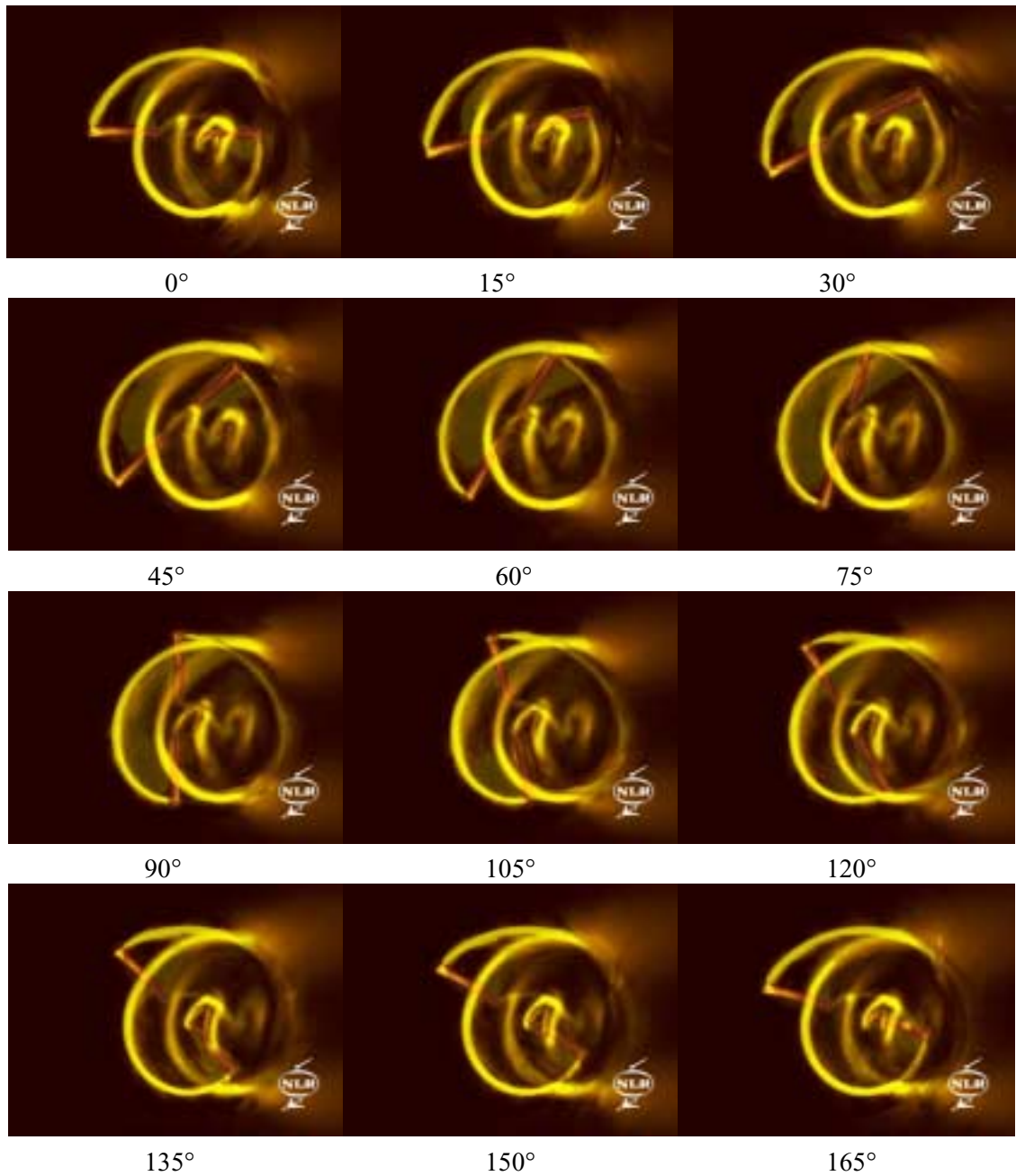
Figure 5: Vorticity magnitude (|ω|) contours for the Operational Loads Survey helicopter rotor in forward flight at azimuthal steps of 15 degrees for Schedule 3. The vorticity magnitude |ω| ranges from 0 to 1. The airflow is from left to right.